

Underwater Source Localization Using an Artificial Lateral Line System With Pressure and Flow Velocity Sensor Fusion

Yonggang Jiang, Zheng Gong^{ID}, Zhen Yang^{ID}, Zhiqiang Ma, Chunxuan Wang, Yanjie Wang, and Deyuan Zhang^{ID}, Member, IEEE

Abstract—Mimicking fish lateral line for hydrodynamic sensing, various artificial lateral line systems have been developed for underwater robotics. However, previous studies of artificial lateral line systems for underwater source localization were based on a single sensing modality of either pressure or flow velocity. Inspired by the functions of flow and pressure receptors of fish, in this article, we developed an artificial lateral line system integrated with pressure sensors and flow velocity sensors. A dual-sensor fusion modality was proposed to locate near-field dipole source by measuring hydrodynamic signals. A multilayer perceptron neural network was constructed to process the pressure and flow velocity signals and to predict near-field dipole coordinates in two and three dimensions. In a 2-D plane, compared with a single pressure- or velocity-sensing modality, the dual-sensor fusion modality reduced the mean localization error by 30%. In a 3-D space, the mean localization error based on the dual-sensor fusion modality was approximately 0.1 body lengths, when considering a source located within one body length from the artificial lateral line. In addition, we studied the influence of the number of sensors on the localization accuracy via analysis of variance. Our experimental results indicated that the bio-inspired dual-sensor fusion modality is beneficial for improving the performance of artificial lateral line systems for underwater source localization.

Index Terms—Artificial lateral line, artificial neural network, biomimetic, localization, sensor fusion.

Manuscript received July 25, 2020; revised January 3, 2021; accepted February 21, 2021. Date of publication March 2, 2021; date of current version February 17, 2022. Recommended by Technical Editor J. Zhang and Senior Editor K. Kyriakopoulos. This work was supported by the National Natural Science Foundation of China under Grant 51575027 and Grant 51975030. (*Corresponding author: Yonggang Jiang*.)

Yonggang Jiang, Zheng Gong, Zhen Yang, Zhiqiang Ma, and Deyuan Zhang are with the School of Mechanical Engineering and Automation, Beihang University, Beijing 100191, China (e-mail: jiangyg@buaa.edu.cn; zhenggong@buaa.edu.cn; godzheny@qq.com; mazqbuaa@163.com; zhangdy@buaa.edu.cn).

Chunxuan Wang is with the Shandong Yihang Brake Technology Company LTD., Shandong 256600, China (e-mail: wdlsd008@163.com).

Yanjie Wang is with the School of Mechanical and Electrical Engineering, Hohai University, Changzhou 213022, China (e-mail: yjwang@hhu.edu.cn).

Color versions of one or more figures in this article are available at <https://doi.org/10.1109/TMECH.2021.3062869>.

Digital Object Identifier 10.1109/TMECH.2021.3062869

I. INTRODUCTION

FISH can accurately sense surrounding flow disturbances via their lateral line systems [1]. These systems influence the behavior of fish [2]–[5], such as schooling, rheotaxis, and obstacle avoidance. The lateral line systems comprise hundreds of sensing units called neuromasts, which can be divided into two categories: superficial neuromasts (SNs) and canal neuromasts (CNs) [6]. SNs sit on the skin and are sensitive to flow velocities. CNs are located with the lateral line canals underneath the skin and are sensitive to the pressure gradients between canal pores [7].

In dark and murky water environments, vision-based underwater vehicles experience difficulty detecting their surroundings. Passive sensing is preferred over traditional detection techniques such as sonar in scenarios considering ecological protection. The ultrasensitive flow perception capability of biological lateral lines has inspired engineers to develop artificial lateral line (ALL) systems. Over the last few decades, ALL systems based on pressure or flow velocity sensors have been developed to perceive near-field hydrodynamic fluctuations and put into applications such as flow control of underwater robots [8] and ecological environmental detection [9]. Extensive studies on ALL systems have been conducted to explore the strategies for vortex sensing [10]–[12] and attitude control [13]–[16]. For instance, Venturelli *et al.* employed a bilateral array of pressure sensors to detect vortex shedding frequency, vortex travelling speed, and downstream distance between vortices [12]. Salumae *et al.* developed a robotic fish equipped with an ALL system for attitude control under steady flow conditions [13]. ALL sensors were used to detect the orientation of the robot with respect to the flow direction; furthermore, using these systems, the standard deviation of error was considerably reduced to 2.9°.

Several studies on ALL systems focus on dipole localization, in addition to vortex detection and attitude control. A dipole-generated flow field closely represents those generated by fins or insects [17]. In practical applications, certain vibrating targets location can be simplified to dipole source localization such as artificial swing fins or propellers installed on an underwater vehicle [18]. Stimulated by this typical source of vibration, the researchers found that the fish showed the ability to locate nearby vibrations and moving objects [17]. In addition, a dipole source is easy to realize and control; such flow fields are commonly

used as a stimulus in lateral line studies. Therefore, dipole localization has been a crucial evaluation criterion for ALL performance. For instance, Abdulsadda *et al.* developed an ALL system with a velocity sensor array to locate the dipole source in a two-dimensional (2-D) space [19]. Yang *et al.* proposed an ALL system comprising 15 flow velocity sensors placed crosswise on a cylindrical platform to locate a vibrating source in a three-dimensional (3-D) space [20]. Zheng *et al.* developed a cross-shaped ALL with nine pressure sensors for 3-D dipole localization [21]. All the above experimental studies on dipole localization involving ALL systems employed single pressure- or velocity-sensing modality. DeVries *et al.* employed a multimodal ALL with both pressure difference and flow velocity sensors for vortex sensing and attitude control [22]. Thus far, to the best of our knowledge, this article is first to present an ALL system that utilizes pressure and flow velocity sensor fusion modality to localize an underwater target.

Various signal-processing approaches have been used to realize dipole source localization [23], including template matching, wavelet transform, beamforming, model-based estimation, and even artificial neural networks. Although it is unknown at present how fish use their central nervous systems to determine source localization, and while the working principle of fish neural networks is different from that of artificial neural networks, previous studies have demonstrated that artificial neural networks provide an efficient technique to deal with this problem [21], [24], [25].

In this article, we proposed an ALL system that integrates pressure and flow velocity sensors to locate near-field dipole sources. Similar to fish lateral line, two sensor arrays were arranged in parallel, where the sensitivity direction of the flow velocity sensor was dorsoventral with respect to the body. Compared to cross-shaped ALL systems and crosswise sensor arrays, our arrangement is more compact and transplantable, especially with regard to streamlined underwater vehicles. Furthermore, based on the dual-sensor fusion modality, we constructed a multilayer perceptron (MLP) neural network algorithm for source localization experiments, which achieved high localization accuracy.

The remainder of this article is organized as follows. The experiment platform and perception algorithm are presented in Section II. The results and discussion of the experiments on dipole 2-D and 3-D dipole localization are introduced in Section III. The concluding remarks are summarized in Section IV.

II. EXPERIMENT PLATFORM AND PERCEPTION ALGORITHM

In this section, we first discuss the analytical model for a dipole-generated flow field and present the complementary arrangement of sensor arrays. We then introduce the design of the ALL system along with the experimental setup. Finally, we describe the MLP architecture for the neural network to process pressure and velocity signals.

A. Flow Field Model of Dipole Source in a 3-D Space

As shown in Fig. 1, the sphere located at (X_D, Y_D, Z_D) vibrates parallel to the z -axis with an instantaneous velocity $v(t) = s\omega \sin(\omega t)$. Here, s is the amplitude of the vibration and

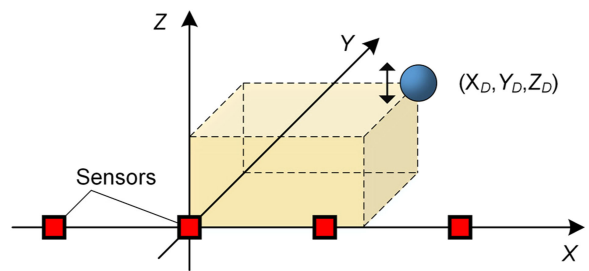


Fig. 1. Schematic of dipole source localization in a 3-D space.

$\omega = 2\pi f$ is the angular frequency. All the sensors lie along the x -axis and the coordinates of sensor_i are $(x_i, 0, 0)$. The pressure $p(i)$ and flow velocity $v_z(i)$ in the z -direction at the position of sensor_i can be calculated as follows [26], [27]:

$$p(i) = \rho \omega a^3 v(t) \frac{|Z_D|}{[Z_D^2 + (x_i - X_D)^2 + Y_D^2]^{3/2}} \quad (1)$$

$$v_z(i) = (2a)^3 v(t) \frac{2Z_D^2 - [(x_i - X_D)^2 + Y_D^2]}{[Z_D^2 + (x_i - X_D)^2 + Y_D^2]^{5/2}} \quad (2)$$

where ρ is the density of water and a is the radius of the sphere. The flow field model of the dipole source provides important guidance for the sensor arrangement of the ALL.

B. Complementary Sensor Array Arrangement

Pressure and velocity signals are usually sampled by sensors with finite precision. Assuming that the minimum detection limits of the pressure sensor and the flow velocity sensor are 1 Pa and 1 mm/s, respectively, the spatial detection range of the two sensors can be calculated according to (1) and (2) under a certain dipole excitation mode. Here, the sphere has a radius $a = 12.5$ mm, which oscillates at a frequency $f = 35$ Hz and has a displacement amplitude $s = 1$ mm. Fig. 2(a) shows the detection range when the pressure sensor is located at the origin. The $R_D = (X^2 D + Y^2 D)^{1/2}$ represents the horizontal distance between the pressure sensor and the sphere. The pressure sensor can detect vibrations when the sphere is located at areas between the red line and the origin. The spatial detection range of the flow velocity sensor located at the origin is shown in Fig. 2(b).

When a dipole is located at the x - y plane, $p(i)$ is calculated to be 0 according to (1). The pressure sensor at the origin cannot provide reliable pressure information; however, the velocity $v_z(i)$ can be used for localization of the dipole source. When the distance between the dipole and the sensor array increases, the magnitude of the velocity decreases rapidly while that of the pressure decreases relatively slowly.

Combining the response characteristics of pressure and flow velocity sensors for dipole excitation, we designed the ALL sensor arrays. Fig. 2(c) shows the arrangement of the sensor arrays and the detection ranges of pressure sensors and velocity sensors. The flow velocity sensor complements the blind area of the pressure sensor, and the pressure sensor extends the spatial detection range. Therefore, flow velocity and pressure data are complementary for dipole localization.

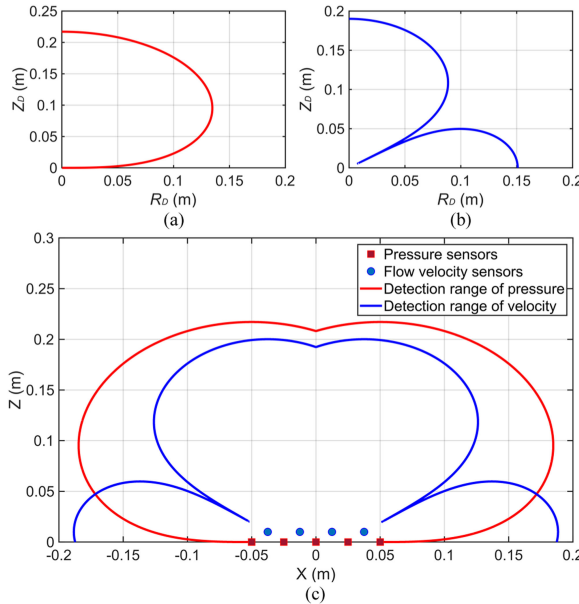


Fig. 2. Sphere detection range calculated according to (1) and (2). (a) Maximum detection range of the pressure sensor at the origin (red curve). (b) Maximum detection range of the flow velocity sensor at the origin (blue curve). (c) Detection range of ALL. The red and blue curves represent the maximum detection ranges of the pressure sensors and flow velocity sensors on both sides, respectively. The figure shows only the detection range of the positive z -axis in the x - z plane.

From (1) and (2), we can infer that the sensor array placed along the x -axis cannot distinguish the sign of the z -coordinate of the dipole, as the pressure or flow velocity output are identical for two dipoles located symmetrically about the x - y plane. The offset placements of pressure and flow velocity sensors contribute to dipole localization in a 3-D space. To solve the symmetry problem of dipole localization in a 3-D space, Wolf *et al.* [28] also chose a sensor array composed of two ALLs with equidistant flow velocity sensors, retaining the ability to make use of spatial properties while allowing the 3-D localization.

C. Design of ALL

Fig. 3 shows the hardware configurations and dimensions of the ALL system. The system comprises a 3-D printed shell, pressure and flow velocity sensor arrays, amplifier circuits, a wireless data acquisition card, a power-supply circuit, and a battery. The body of the ALL system is 27 cm in length (L) and 9 cm in diameter (D). On one side of the body, five pressure sensors and four flow velocity sensors were installed at equal intervals ($S_P = S_V = 25$ mm) along the rostrocaudal direction of the body, as shown in Fig. 3(b). The horizontal interval (S_s) between adjacent pressure and flow velocity sensors was 12.5 mm. In our study the body length (BL) was defined as the length of the maximum length of the sensor array, $BL = 100$ mm. The CNs and SNs of the lateral line of fish were not distributed in a straight line [29]; furthermore, as described in Section II-A, their offset was conducive to locating dipoles in a 3-D space. Based on this arrangement, we set a 10 mm row spacing (H) between the pressure sensor array and the flow velocity sensor array.

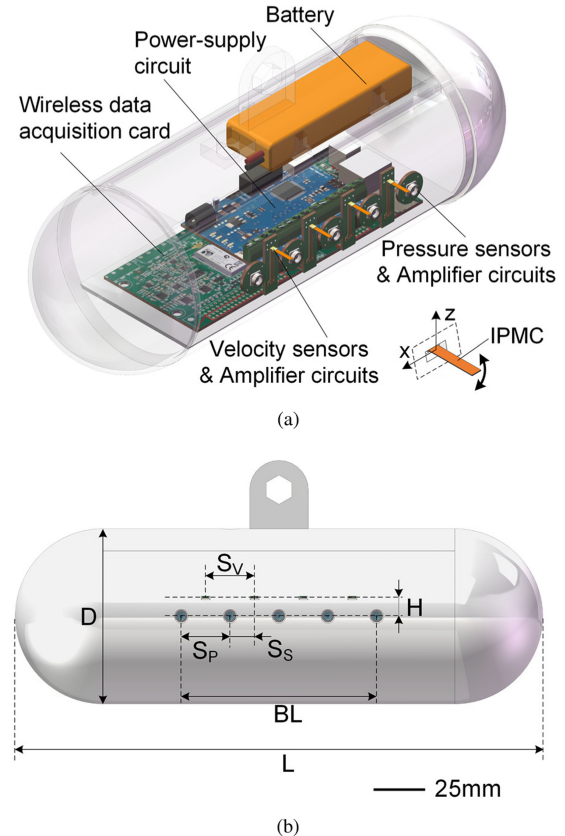


Fig. 3. ALL system with pressure and flow velocity sensors. (a) Transparent view: internal hardware configuration. (b) Front view: overall dimensions of the model.

Pressure sensors (MS5401-AM, Measurement Specialties Inc., USA) fixed on the surface of the body with a waterproof sealant were used to measure the absolute pressure. Each sensor was equipped with a voltage amplifier circuit, which comprised two instrumentation amplifiers (INA) with a gain of 500.

Ionic polymer–metal composite (IPMC) is an important class of electroactive polymers with inherent actuation and sensing properties [30], [31] and has been widely used for underwater actuation [32], perception [33], and energy collection [34]. Owing to the advantages of simple fabrication processing with soft materials and high sensitivity, an IPMC beam was designed for flow velocity sensing. Each IPMC sensor had a specification of $10 \text{ mm} \times 2 \text{ mm} \times 0.2 \text{ mm}$. Similar to the SNs of fish, the IPMC sensors bent along the dorsoventral direction of the body to measure flow velocity along the z -direction. IPMC sensors were fixed on the body with a waterproof sealant. To ensure the stability of water content inside the material, the IPMC surface was uniformly coated with silicone gel (Ecoflex 00-10, Smooth-On, Inc., USA) with a low modulus of elasticity. An IPMC sensor can generate an open-circuit voltage or a short-circuit current across two electrodes under mechanical stimulation. Previous studies have demonstrated that the voltage output is more accurate than the current output for the dynamic response of oscillating displacement [35]. Therefore, we selected an open-circuit voltage as the sensor output. Fig. 4(b) shows the schematic diagram of the voltage amplifier circuit for each IPMC

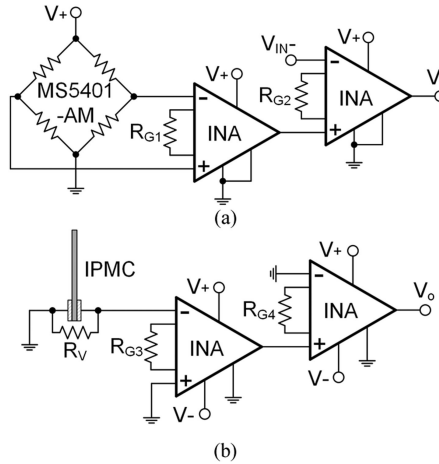


Fig. 4. Schematic of the voltage amplifier circuits for pressure sensor (a) and IPMC based flow velocity sensor (b). In the circuits $R_{G1} = 10 \text{ k}\Omega$, $R_{G2} = R_{G3} = R_{G4} = R_V = 2 \text{ k}\Omega$.

sensor with a gain of 2500. All pressure and velocity signals were input into the wireless data acquisition card (T7-Pro, Labjack Co., USA) communicating with the host computer; these signals were then recorded. Nine data channels worked synchronously at a sampling frequency of 300 Hz with a digitization accuracy of 16 bit.

D. Experimental Setup

All experiments were conducted in an open water flume with an experimental section of $70 \times 35 \times 40 \text{ cm}^3$ (length \times width \times height), filled with water to a depth of 30 cm, as shown in Fig. 5. The ALL system was connected to a two-axis sliding table and was moved to the center of the flume (diving depth 15 cm) for localization experiments. The sphere with a diameter of 25 mm was connected to the vibrator through a stainless-steel rod 200 mm in length and 5 mm in diameter, which vibrated sinusoidally in the vertical direction with a variable vibration amplitude and frequency. The vibrator was installed on a three-axis sliding table regulating the position of the dipole in a 3-D space. The two gantry shelves and the flume were not in contact with each other, which can avoid the noise caused by vibration. This study selected a vibration frequency of 35 Hz, which is in the typical range for the dipole localization study of the ALL. The dipole vibration direction of all the experiments was perpendicular to the water surface, with an amplitude of 1 mm.

E. Sensor Calibration

To ensure the accuracy of the pressure signals for the dipole localization, we calibrated all the pressure sensors. Specifically, we dived the ALL systems at different depths underwater and recorded the corresponding output voltage signals. The output voltage of the first pressure sensor (P_1) exhibited a linear relationship with the pressure variation, as shown in Fig. 6. The calibration results for the sensitivity of all the pressure sensors are listed in Table I.

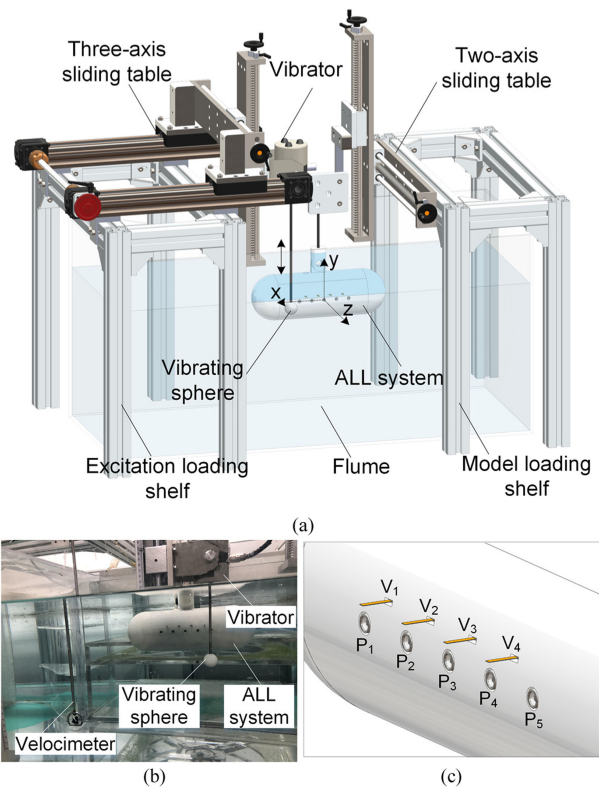


Fig. 5. Experiment setup of dipole localization. (a) Components of the experimental setup. (b) Photography of the established platform. (c) Number of pressure and flow velocity sensors.

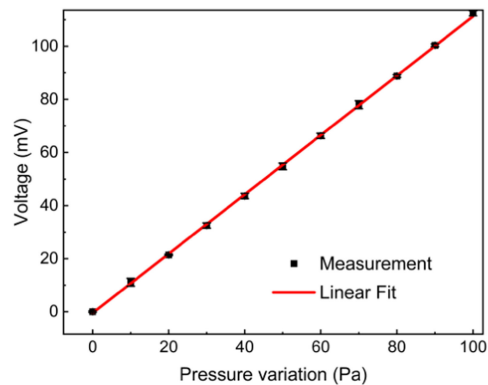


Fig. 6. Calibration of a representative pressure sensor (P_1).

TABLE I
PROPORTIONALITY CONSTANTS OF ALL SENSORS
IDENTIFIED BY LINEAR FITTING

Pressure sensor number	Proportional constant k_p (mV/Pa)	Flow velocity sensor number	Proportional constant k_v (mV/(mm s ⁻¹))
P_1	1.12	V_1	3.64
P_2	1.17	V_2	2.04
P_3	1.15	V_3	3.66
P_4	1.22	V_4	2.95
P_5	1.24		

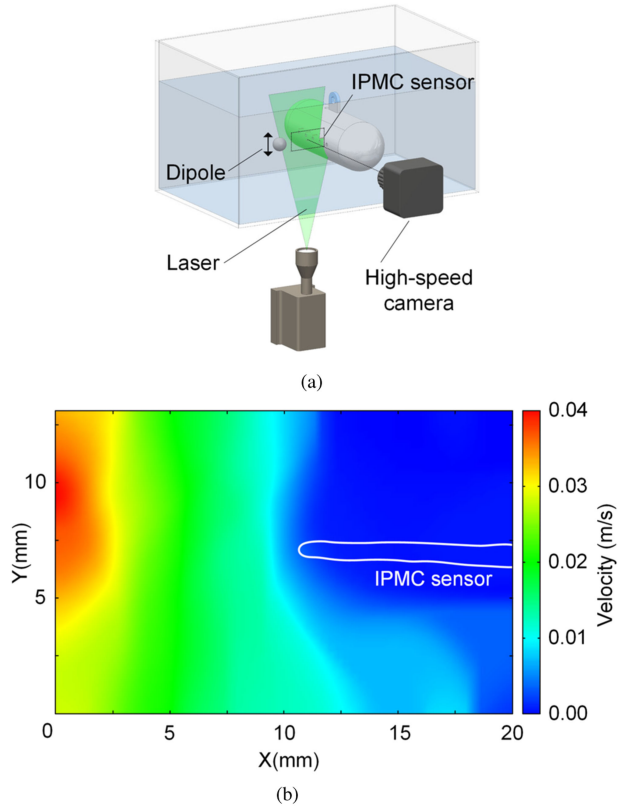


Fig. 7. Calibration of IPMC sensors with a PIV system. (a) Schematic of the experimental setup. (b) Velocity field around the fourth IPMC sensor (V_4) under a dipole stimulation.

The relationship between the voltage output of the IPMC sensor and local flow velocity can be established via a fluid-structure interaction analysis. However, the final output of different IPMC sensors varies because of the inhomogeneity of the material, subtle difference in dimensions, and deviation of electrical parameters. To determine the accuracy of the flow velocity signal, this study employed a particle image velocimetry (PIV) system to calibrate each IPMC sensor, as shown in Fig. 7(a). Considering the fourth IPMC sensor (V_4) as an example, the laser illuminated the vertical plane, where the cantilever beam and dipole were located to visualize the movement of tiny particles in the water under the excitation of the dipole.

Fig. 7(b) shows the velocity distribution near the tip of the IPMC sensor, when the dipole was 50 mm away from the sensor. The dipole vibration conditions in the calibration experiment were the same as those described in Section II-C. By analyzing the flow field at different points between dipole and the IPMC sensor apex, we obtained a series of IPMC sensor tip flow velocity amplitudes and the corresponding voltage signal amplitudes. As shown in Fig. 8, the peak-to-peak voltage output of the IPMC sensor was approximately linear with the amplitude of the flow velocity within a certain range. Table I lists the sensitivity calibration results of all IPMC sensors.

F. Neural Network Algorithm for Dipole Localization

Previous work focused on establishing a perception model for dipole localization in which flow field conditions were idealized

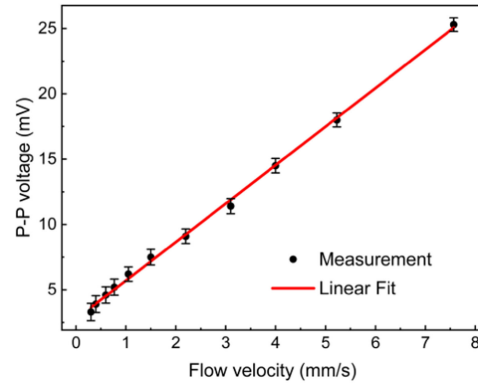


Fig. 8. Calibration of a representative IPMC based flow velocity sensor (V_4).

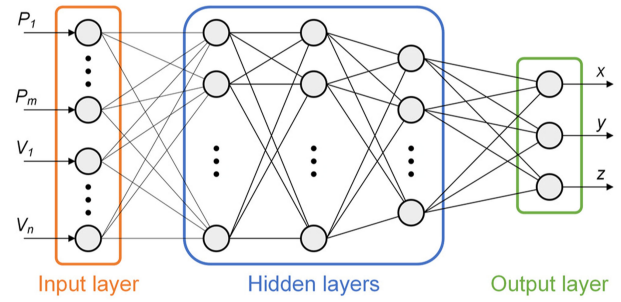


Fig. 9. Schematic of the MLP neural network for signal processing of the ALL. The input parameters are pressure or velocity amplitudes, and the output nodes represent the predicted dipole coordinates.

[26]. In an actual flow field, several uncontrollable factors, such as noise and interference derived from the interaction of the fluid with the shell of the ALL and the flume wall, cause the actual sensor to generate an output that is significantly different from the theoretical result. As a result, it is difficult to directly calculate the dipole coordinates via an analytical method. Artificial neural networks are capable of nonlinear regression and are compatible with multiple data inputs, which can predict the dipole position by training on certain data. Therefore, we constructed an artificial neural network to process signals from sensors. As shown in Fig. 9, the MLP is a feedforward artificial neural network model comprising an input layer, several hidden layers, and an output layer. Owing to its simple structure, adaptive learning ability, noise robustness [36], and wide application in nonlinear classification and regression [37], we adopted a signal processing method based on MLP.

In general, it is necessary to preprocess the obtained pressure and flow velocity signals, extract the characteristic values, and input them into the neural network after standardization. Fig. 10 shows a typical set of signals preprocessing. Because the dipole vibration is periodic, the voltage outputs of the sensors are continuous sinusoidal signals. For each run in all the experiments, the signals from ALL were recorded for 30 s, and fast Fourier transform (FFT) was employed to extract the amplitude of each signal at 35 Hz, which was then multiplied by the sensitivity of the corresponding sensor to obtain the pressure amplitude and velocity amplitude. These amplitudes reflect the characteristics of the dipole flow field, and immunity to noise

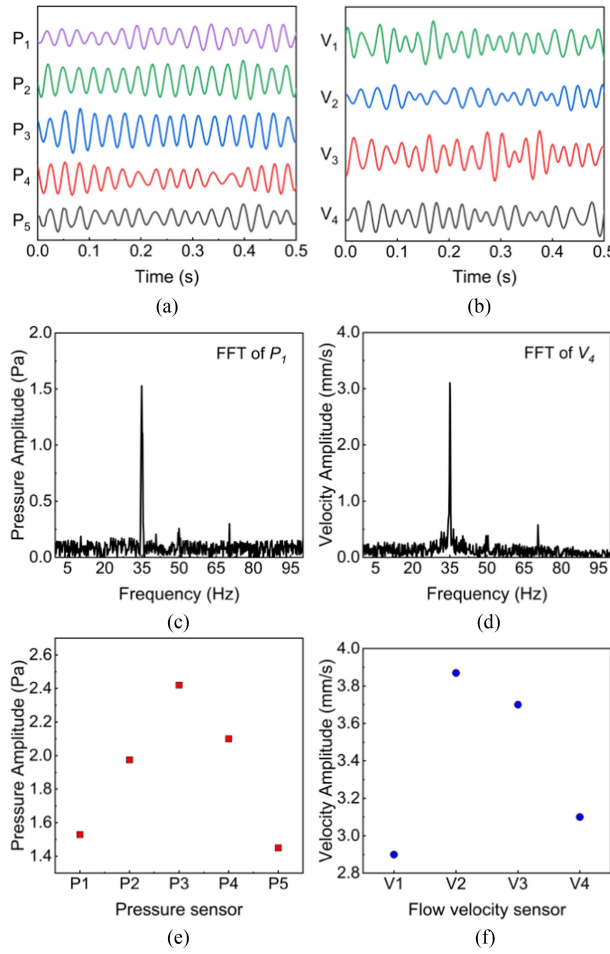


Fig. 10. When the dipole sphere was located at (0, 80, -30 mm): the time-domain signals of pressure sensors (a) and flow velocity sensors (b), the frequency-domain signals of pressure sensor P_1 (c) and flow velocity sensor V_4 (d) transformed by FFT, and the vibration signal amplitudes at 35 Hz for pressure sensors (e) and flow velocity sensors (f).

can be improved through amplitude extraction. Fig. 10(e) and (f) show the vibration signal amplitudes of pressure sensors and flow velocity sensors when the dipole sphere was located at (0, 80, -30 mm).

MLP is performed as a series of weighted calculations on the input. Direct input of the pressure and velocity signals into the neural network leads to difficulty in model convergence or large errors in prediction results due to the difference of the signal dimensions. To remove the influence of data dimensionality on the neural network and accelerate the convergence of MLP, it is necessary to standardize the signal amplitudes. Therefore, the standardized signal amplitude $S_j^*(i)$ can be derived by the following:

$$S_j^*(i) = \frac{S_j(i) - S_j(M)}{S_j(\sigma)}. \quad (3)$$

Here, $S_j(i)$ denotes the signal amplitude i of sensor j , and $S_j(M)$ and $S_j(\sigma)$ represent the mean and standard deviation of sensor j in the signal amplitude sample, respectively. For each pressure or flow velocity sensor, the mean value and variance of the training points are 0 and 1 after standardization, respectively.

Finally, the standardized signal amplitudes were used as the input of the neural network.

In addition, the number of input nodes in the neural network is equal to the number of sensors, and each output node represents the predicted coordinates of the dipole on each axis. Node activation values can be computed by the following [36]:

$$a_j^l = f \left(\sum_{k=1}^N w_{jk}^l a_k^{l-1} + b_j^l \right). \quad (4)$$

Here, a_j^l denotes the activation of the j th node of the l th layer, where counting starts at the first hidden layer. We use w_{jk}^l to denote the weight of the connection from the k th node in the $(l-1)$ th layer to the j th node in the l th layer, and use b_j^l for the bias of the j th node in the l th layer. Furthermore, N denotes the number of nodes in the $(l-1)$ th layer. Each hidden layer node represents a nonlinear activation, which takes the rectified linear unit (ReLU) $f(x) = \max(0, x)$ as the activation function.

The training set of the localization experiment includes a series of known dipole coordinates and the corresponding pressure or velocity amplitude from the sensors. Parameters such as the number of hidden layers and nodes and learning rate are obtained via training.

The absolute localization error can directly reflect the performance of dipole localization by ALL. The absolute error along each axis can be expressed by the difference between the actual and predicted values. The absolute localization error in 2-D and 3-D spaces can be expressed using Euclidean distance (ED) as follows:

$$ED = \sqrt{(x_i - X_i)^2 + (y_i - Y_i)^2} \quad (5)$$

$$ED = \sqrt{(x_i - X_i)^2 + (y_i - Y_i)^2 + (z_i - Z_i)^2} \quad (6)$$

where (x_i, y_i) and (x_i, y_i, z_i) represent the predicted coordinates in 2-D and 3-D spaces, respectively, and (X_i, Y_i) , (X_i, Y_i, Z_i) represent the actual coordinates.

III. RESULTS AND DISCUSSIONS

This section presents the experimental results of dipole localization. The modality of dual-sensor fusion achieves a higher localization accuracy than single sensing modality. The 2-D localization results described in Section III-A can intuitively illustrate this advantage. Furthermore, the ALL system with the modality of dual-sensor fusion demonstrates the ability to locate dipoles in the 3-D space, and the results are described in Section III-B. In Section III-C, we use the ANOVA to consider the influence of the number of pressure sensors and flow velocity sensors on the localization accuracy. Finally, we investigate how ambient water flow affects the localization accuracy in Section III-D.

A. Dipole Source Localization in 2-D Plane

We performed dipole localization experiments in a 2-D plane, on which the four IPMC sensors were placed. For the convenience of description, we took the midpoint of the flow velocity sensor array as the origin to establish the coordinate system. To train the neural network, the plane ($100 \times 50 \text{ mm}^2$) was divided

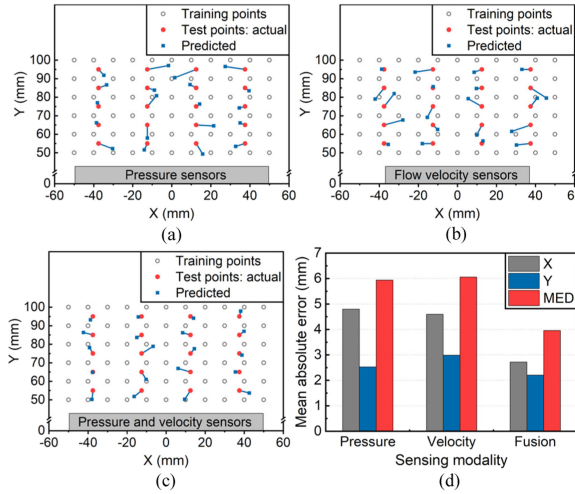


Fig. 11. Experimental results of dipole localization in 2-D space. (a) Localization results by using pressure-sensing modality. (b) Localization results by using velocity-sensing modality. (c) Localization results by using dual-sensor fusion modality. (d) Comparison of the mean absolute error along x - and y -axes and the MED of test points for the three sensing modalities.

into a grid of $10 \times 10 \text{ mm}^2$ lattices, forming 66 training points, as shown in Fig. 11. The dipole was placed at each training point, and the obtained sensor signals were used to train the neural network. Then, the dipole was placed at each of the 20 test points and the obtained velocity or pressure amplitude was input into the neural network to predict the corresponding coordinates. The parameters of the neural network were then determined after training for 1000 epochs. The optimal MLP network architecture had two hidden layers of 100 and 50 nodes, respectively. The learning rate was set to 0.002.

Fig. 11(a)–(c) show the experimental results of dipole localization using pressure-sensing modality, velocity-sensing modality, and dual-sensor fusion modality, respectively. The red dots and blue dots represent the actual and predicted positions of the test points, respectively. As summarized in Fig. 11(d), when pressure- or velocity-sensing modality is used, the mean Euclidean distance (MED), mean absolute error along the x -axis (MAE-X), and mean absolute error along the y -axis (MAE-Y) are approximately 6, 5, and 3 mm, respectively. Furthermore, when the dual-sensor fusion modality is employed, the MED, MAE-X, and MAE-Y are attenuated to approximately 4, 2.7, and 2.2 mm, respectively. Based on the results of 2-D dipole localization, we can conclude that the localization accuracy with dual-sensor fusion modality is much higher than that with the single sensing modality.

B. Dipole Source Localization in 3-D Space

We performed a 3-D dipole localization experiment to verify the performance of dual-sensor fusion modality. The position of the third pressure sensor (P_3) was taken as the origin to establish the coordinate system and a 3-D space ($100 \times 50 \times 100 \text{ mm}^3$) was defined. As shown in Fig. 12, we divided the space into a grid of $10 \times 10 \times 10 \text{ mm}^3$ lattices, forming 726 grid points as the training points. In the working space, 81 test points that were excluded from the training points were set along the

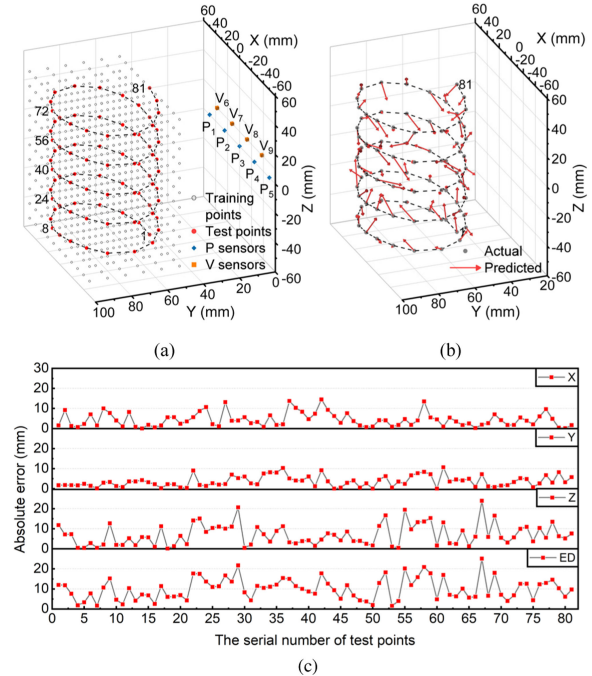


Fig. 12. Dipole localization in 3-D space using dual-sensor fusion modality. (a) 726 training points and 81 test points. (b) Predicted and actual positions of all test points. (c) Absolute error along the three axes and the ED for all test points between the predicted and the actual.

elliptical spiral trajectory. Fig. 12(a) shows the relative positions of the training points, the test points, and all the sensors of ALL. We determined the parameters of the neural network after training for 2500 epochs. The optimal MLP network architecture had three hidden layers, which are 100, 100, and 50 nodes, respectively. The learning rate was set at 0.0025.

Fig. 12(b) shows the actual and predicted positions of all test points. To illustrate the relative position clearly, we use gray dots to represent the actual coordinates, and the arrows point to represent the corresponding predicted coordinates. Fig. 12(c) shows the absolute errors for 81 test points between the predicted and actual positions. From the viewpoint of statistics, the MAEs along the x -, y -, and z -axes are 4.3, 3.6, and 7.0 mm, respectively. The MED between the predicted coordinates and actual coordinates is 10.0 mm, which is dominated by the z -axis error.

In Zheng's dipole localization study [21], within 0.6 BL away from the ALL, the MAEs along the x -, y -, and z -axes were 7.1, 4, and 3.2 mm, respectively. Furthermore, in Yang's study [20], a mean localization error of 0.17 BL was obtained when the distance between the dipole and ALL was 0.5 BL. Therefore, compared to state-of-the-art techniques used for dipole localization, our system with the dual-sensor fusion modality achieves higher localization accuracy within a larger dipole-sensor distance.

C. Effect of Sensor Type and Number on Localization Error

ANOVA is a statistical technique for analyzing the effects of several factors on the means of variables and identifying

TABLE II
COMBINATIONS OF DIFFERENT NUMBERS OF PRESSURE AND FLOW VELOCITY SENSORS FOR DIPOLE LOCALIZATION

	V_{num}		
P_{num}	2	3	4
2	$P_{2,4} + V_{2,3}$	$P_{2,4} + (V_{1,2,3} \text{ or } V_{2,3,4})$	$P_{2,4} + V_{1,2,3,4}$
3	$P_{2,3,4} + V_{2,3}$	$P_{2,3,4} + (V_{1,2,3} \text{ or } V_{2,3,4})$	$P_{2,3,4} + V_{1,2,3,4}$
4	$P_{1,2,4,5} + V_{2,3}$	$P_{1,2,4,5} + (V_{1,2,3} \text{ or } V_{2,3,4})$	$P_{1,2,4,5} + V_{1,2,3,4}$
5	$P_{1,2,3,4,5} + V_{2,3}$	$P_{1,2,3,4,5} + (V_{1,2,3} \text{ or } V_{2,3,4})$	$P_{1,2,3,4,5} + V_{1,2,3,4}$

any interactions between the factors [38], [39]. We utilize a two-way ANOVA to evaluate the influence of the two factors, the number of pressure sensors (P_{num}) and the number of flow velocity sensors (V_{num}), on the localization error and identify if the interaction between the two factors is significant. Notably, P_{num} has four levels: 2, 3, 4, or 5. V_{num} has three levels: 2, 3, or 4. We consider 12 combinations of P_{num} and V_{num} , as presented in Table II. We repeated each combination 10 times and recorded all the experimental results. The number of input nodes was equal to the number of sensors and other parameters of the MLP neural network were the same as in the localization experiment in a 3-D space. It should be pointed out that when V_{num} is 3, $V_{1,23}$ and $V_{2,34}$ are used for five trials each. Meanwhile, the localization error is discussed according to the four variables of the MAE along the x -, y -, and z -axes and the MED.

The underlying assumptions for ANOVA are that data samples satisfy normal distribution and homogeneity of variance. Violations of these assumptions may invalidate the ANOVA results. The Shapiro-Wilk test [40] can be used to test the normality of samples with data less than 2000. Levene's test [41] is widely used to test the homogeneity of variances. At the significance level of 0.05, the test results showed that the data are approximately normally distributed ($P > 0.05$), and variances were homogeneous ($p > 0.05$). In addition, there are no outliers (the observation is more than two standard deviations from the mean) in the data. Therefore, we can conclude that the experiment data satisfy underlying assumptions of ANOVA.

The results of ANOVA for the localization error are presented in Table III. For all the indicators of the localization error, the main effects of P_{num} and V_{num} are observed to be highly significant ($P < 0.001$). For MAE-X and MED, the interaction between P_{num} and V_{num} is significant ($P < 0.05$), but not for MAE-Y and MAE-Z ($P > 0.05$). Therefore, the effects of P_{num} and V_{num} on MAE-Y and MAE-Z can be analyzed directly according to their respective main effects. However, for P_{num} (or V_{num}) at different levels, the effect of V_{num} (or P_{num}) on MAE-X and MED should be analyzed separately [42].

Fig. 13(a) and (b) show MAE-X under each combination studied. When two or three flow velocity sensors are used, MAE-X decreases with the increase of P_{num} . When four flow velocity sensors are combined with four or five pressure sensors, their MAE-Xs are approximately equal. It indicates that an additional increase in the number of pressure sensors may not significantly reduce MAE-X when four flow velocity sensors are used. However, when four or five pressure sensors are used, the error decreases with the increase in V_{num} .

TABLE III
EFFECTS OF P_{num} AND V_{num} ON THE LOCALIZATION ERROR OF THE ALL SYSTEM IN 3-D SPACE

Source	SS	df	MS	F	P
Mean absolute error along the x-axis					
P_{num}	28.687	3	9.562	133.417	<0.001
V_{num}	35.020	2	17.510	244.309	<0.001
$P_{num} \times V_{num}$	1.517	6	0.253	3.528	0.003
Residual	7.741	108	0.072		
Mean absolute error along the y-axis					
P_{num}	12.709	3	4.236	52.376	<0.001
V_{num}	4.536	2	2.268	28.041	<0.001
$P_{num} \times V_{num}$	0.490	6	0.082	1.009	0.424
Residual	8.735	108	0.081		
Mean absolute error along the z-axis					
P_{num}	639.228	3	213.076	1003.951	<0.001
V_{num}	7.903	2	3.952	18.619	<0.001
$P_{num} \times V_{num}$	1.072	6	0.179	0.842	0.541
Residual	22.922	108	0.212		
MED					
P_{num}	694.737	3	231.579	1361.858	<0.001
V_{num}	58.948	2	29.474	173.329	<0.001
$P_{num} \times V_{num}$	2.398	6	0.400	2.350	0.036
Residual	18.365	108	0.170		

SS, sums of squares; df, degrees of freedom; MS, mean squares; F, test statistic; P, probability value.

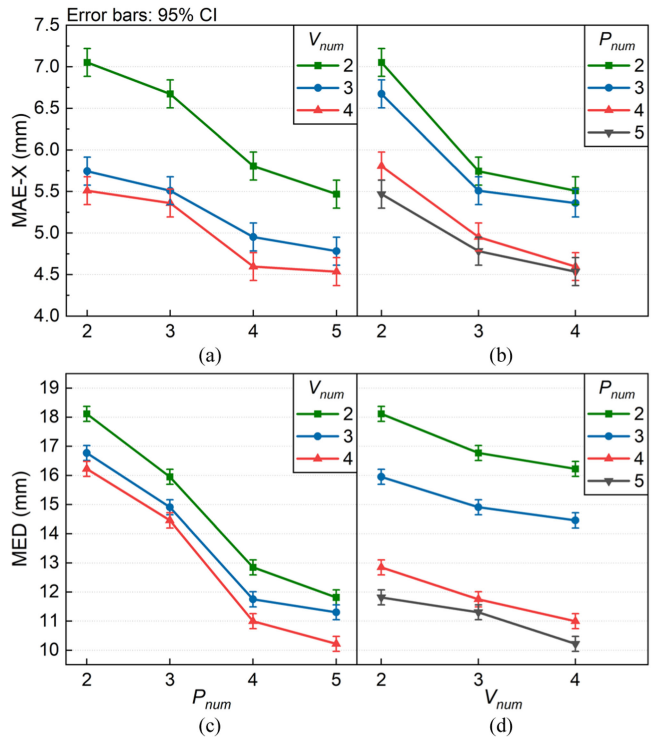


Fig. 13. Mean absolute error along the x -axis (a), (b) and the MED (c), (d) of each combination. Error bars represent 95% confidence interval (CI) for the mean error.

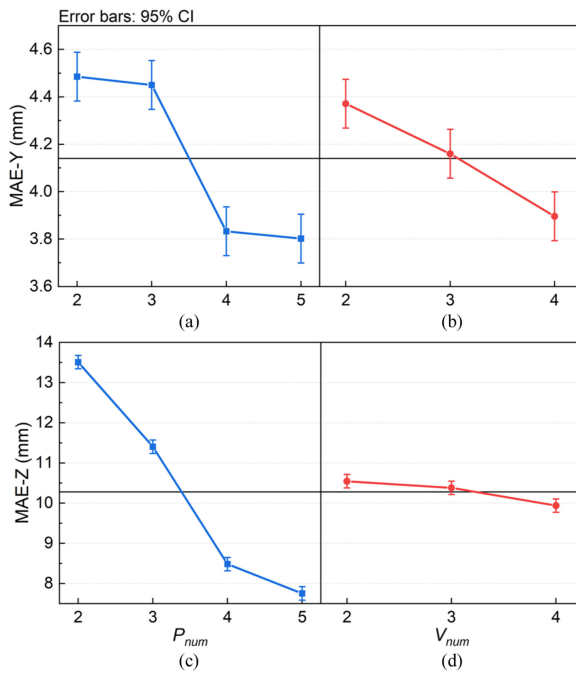


Fig. 14. Main effects of P_{num} and V_{num} for mean absolute error along (a), (b) the y -axis and (c), (d) the z -axis. Error bars represent 95% confidence interval (CI) for the mean error.

The MEDs under each combination are shown in Fig. 13(c) and (d). Under a fixed number of flow velocity sensors, the MED decreases with the increase of P_{num} . When four or five pressure sensors are used, the MED decreases with the increase of V_{num} . In addition, the MED with the combination of five pressure sensors and four flow velocity sensors is 10.2 mm. Therefore, in a 3-D space, within 1 BL from the ALL, the mean localization error is approximately 0.1 BL.

Because the influence of the interaction between P_{num} and V_{num} on MAE-Y and MAE-Z is not significant, we conducted the main effect analysis on P_{num} and V_{num} , as shown in Fig. 14. When P_{num} increases from three to four, MAE-Y decreases significantly; however, it appears that increasing P_{num} from four to five has negligible effect on the MAE-Y. However, as V_{num} increases, the MAE-Y decreases almost linearly. The main effect identified in our analysis of P_{num} and V_{num} on the MAE-Z is illustrated in Fig. 14(c) and (d). Clearly, MAE-Z is mainly affected by the number of pressure sensors. In contrast, increasing V_{num} does not significantly reduce the MAE-Z.

Regardless of the combination used, the localization error always follows the same rule: the MAE-Z is the largest, and the MAE-Y is the smallest. The results of ANOVA show the obvious influence of the number of pressure and flow velocity sensors on the localization accuracy. We find that the MAE-X is significantly affected by the interaction between P_{num} and V_{num} . The flow velocity sensor shows a better tendency to reduce MAE-Y, but the pressure sensor contributes to improving localization along the z -axis, which reflects the complementarity of the dual-sensor fusion modality. The current analysis results provide guidance for the improvement of the ALL system: to improve localization accuracy along the x - and y -axes requires the addition of flow velocity sensors, and to improve accuracy

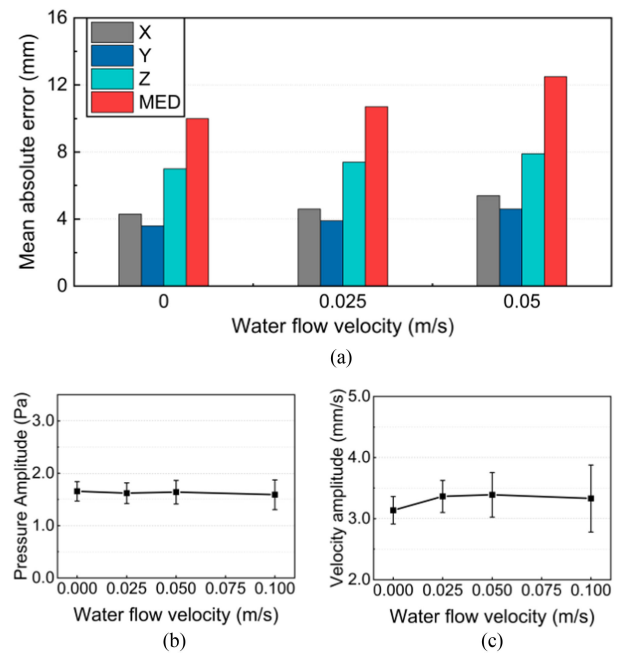


Fig. 15. Under different ambient flow velocities. (a) Comparison of the mean absolute error along x , y , and z -axes and the MED of 81 test points; and (b), (c) when the sphere was located at (0, 80, -30 mm), the vibration signal amplitudes at 35 Hz for pressure sensor P_1 and flow velocity sensor V_4 .

along the z -axis requires the addition of pressure sensors. In addition, the combination of four pressure sensors and four flow velocity sensors is optimal in consideration of minimizing the number of sensors and ensuring high localization accuracy.

D. Effect of Ambient Flow on Localization Error

To investigate the effect of ambient flow on localization accuracy, dipole source localization was performed at different flow velocities. Uniform water flow was set along the negative direction of the x -axis in the flume of the experiment setup shown in Fig. 3, and the flow velocity was measured by a fiber optic velocimeter (SLD300-A, SENLOD, Co. LTD., CHN). We selected two typical flow velocities of 0.025 m/s (1/4 BL/s) and 0.05 m/s (1/2 BL/s). The dipole vibration excitation, training points, test points, and parameters of the MLP neural network were the same as in the localization experiment in the 3-D space.

As shown in Fig. 15(a), when the flow velocity was 0.025 m/s, the MED, MAE-X, MAE-Y, and MAE-Z were approximately 10.7, 4.6, 3.9, and 7.4 mm, respectively, corresponding to 7.0%, 6.9%, 8.3%, 5.7% increase compared to the results in still water. When the flow velocity increased to 0.05 m/s, the MED, MAE-X, MAE-Y, and MAE-Z increased by 25.0%, 25.5%, 27.6%, and 12.8%, respectively. It indicated that high-velocity ambient flow severely deteriorates the localization accuracy and the influence of ambient flow to localization accuracy is mainly reflected in the directions along the x - and y -axes.

To investigate how ambient water flow affects the localization accuracy, we characterized the responses of pressure sensors and velocity sensors to vibration excitations at different flow velocities. When the dipole vibrates at 35 Hz, the signal amplitudes

of the pressure sensor (P_1) and the IPMC flow sensor (V_4) were obtained as shown in Fig. 15(b) and (c), with 15 measurements for each condition. Compared with the flow velocity sensor, the pressure sensor exhibited more stable signal output, which probably explained the insignificant flow impact on MAE-Z even at high flow velocities. When the ambient flow velocity increased to 0.05 m/s, the variance of the velocity amplitude increased by approximately 45%; this was probably the main factor causing the increase of MAE-X and MAE-Y. The disturbance of the ambient flow to velocity sensor signal was significant, though the flow velocity sensor was sensitive in the z -axis (perpendicular to the flow direction). This originated from the inevitable twisting of the long IPMC beam during fabrication as well as installation error. It should be noted that the localization error in flowing water can be reduced by improving the flow sensor stability.

IV. CONCLUSION

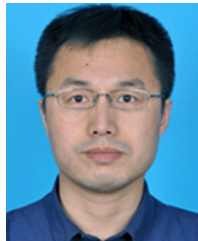
This study introduced an ALL system integrated with pressure and flow velocity sensors along with an MLP neural network to realize the localization of an underwater dipole source. Compared with current single-mode ALL systems, the multimodal ALL system avoids the blind area of the single pressure sensor array and realizes a complementary detection range. In addition, our sensor placement occupies less vehicle area than cross-shaped ALL system, offering better practicality. Based on the results of a 2-D localization experiment, we proved that the dual-sensor fusion modality achieved better performance than the single pressure- or velocity-sensing modality. The results of a 3-D localization experiment showed that the mean localization error between the predicted coordinates of the dipole and the real coordinates was approximately 0.1 BL with a distance of 1 BL. The detection distance of the ALL system is related to the minimum detection limit of the sensor and the excitation intensity of the target source. Although our experiments were done within 1 BL, the localization range can be improved by using high-performance pressure and flow velocity sensors.

Standardization can remove the dimensional effects of the data while preserving the distribution of the data, illustrating good compatibility of the MLP neural network with pressure and flow velocity signals. The MLP neural network can integrate the pressure and flow sensor signals to predict dipole coordinates with high accuracy. However, the disadvantage of this method is that it requires a considerable amount of data to train the neural network. In future work, the complementary effects of pressure and velocity information from the perspective of fluid mechanics can be investigated to provide a more convincing theoretical basis for this approach.

REFERENCES

- [1] S. Dijkgraaf, "The functioning and significance of the lateral line organs," *Biol. Rev.*, vol. 38, pp. 51–105, Feb. 1963.
- [2] H. Bleckmann, "Reception of hydrodynamic stimuli in aquatic and semi-aquatic animals," in *Progress in Zoology*, W. Rathmayer, Ed., Portland, OR, USA: Gustav Fischer, 1994, pp. 1–115.
- [3] Y. Jiang, Z. Ma, and D. Zhang, "Flow field perception based on the fish lateral line system," *Bioinspiration Biomimetics*, vol. 14, no. 4, Jul. 2019, Art. no. 041001.
- [4] T. J. Pitcher, B. L. Partridge, and C. S. Wardle, "A blind fish can school," *Science*, vol. 194, no. 4268, pp. 963–965, Nov. 1976.
- [5] M. J. Kanter and S. Coombs, "Rheotaxis and prey detection in uniform currents by lake michigan mottled sculpin (*Cottus bairdi*)," *J. Exp. Biol.*, vol. 206, no. 1, pp. 59–70, Jan. 2003.
- [6] J. Goulet, J. Engelmann, B. P. Chagnaud, J. M. P. Franosch, M. D. Suttnar, and J. L. Van Hemmen, "Object localization through the lateral line system of fish: Theory and experiment," *J. Comparative Physiol. A, Neuroethol. Sensory Neural Behav. Physiol.*, vol. 194, no. 1, pp. 1–17, Jan. 2008.
- [7] A. Kroese and N. Schellart, "Velocity and acceleration-sensitive units in the trunk lateral line of the trout," *J. Neurophysiol.*, vol. 68, no. 6, pp. 2212–2221, Dec. 1992.
- [8] X. Zheng, W. Wei, M. Xiong, and G. Xie, "Online state estimation of a fin-actuated underwater robot using artificial lateral line system," *IEEE/ASME Trans. Robot.*, vol. 36, no. 2, pp. 472–487, Apr. 2020.
- [9] J. Tuhtan *et al.*, "Man-made flows from a fish's perspective: Autonomous classification of turbulent fishway flows with field data collected using an artificial lateral line," *Bioinspiration Biomimetics*, vol. 13, no. 4, Jul. 2018, Art. no. 046006.
- [10] A. Klein and H. Bleckmann, "Determination of object position, vortex shedding frequency and flow velocity using artificial lateral line canals," *Beilstein J. Nanotechnol.*, vol. 2, pp. 276–283, Jun. 2011.
- [11] Z. Ren and K. Mohseni, "A model of the lateral line of fish for vortex sensing," *Bioinspiration Biomimetics*, vol. 7, no. 3, Sep. 2012, Art. no. 036016.
- [12] R. Venturelli *et al.*, "Hydrodynamic pressure sensing with an artificial lateral line in steady and unsteady flows," *Bioinspiration Biomimetics*, vol. 7, no. 3, Sep. 2012, Art. no. 036004.
- [13] T. Salumae and M. Kruusmaa, "Flow-relative control of an underwater robot," *Proc. Roy. Soc. A, Math. Phys.*, vol. 469, no. 2153, May 2013, Art. no. 20120671.
- [14] Y. Xu and K. Mohseni, "Fish lateral line inspired hydrodynamic force estimation for autonomous underwater vehicle control," in *Proc. 52nd IEEE Conf. Decis. Control*, 2013, pp. 6156–6161.
- [15] L. DeVries and D. A. Paley, "Observability-based optimization for flow sensing and control of an underwater vehicle in a uniform flowfield," in *Proc. Amer. Control Conf.*, 2013, pp. 1386–1391.
- [16] J. Zheng, X. Zheng, T. Zhang, M. Xiong, and G. Xie, "Dual-sensor fusion based attitude holding of a fin-actuated robotic fish," *Bioinspiration Biomimetics*, vol. 15, no. 4, Jul. 2020, Art. no. 046003.
- [17] S. Coombs and R. A. Conley, "Dipole source localization by mottled sculpin: I. Approach strategies," *J. Comput. Physiol. A*, vol. 180, no. 4, pp. 387–399, Apr. 1997.
- [18] M. Ji *et al.*, "Resolution improvement of dipole source localization for artificial lateral lines based on multiple signal classification," *Bioinspiration Biomimetics*, vol. 14, no. 1, Jan. 2018, Art. no. 016016.
- [19] A. T. Abdulsadda and X. Tan, "Nonlinear estimation-based dipole source localization for artificial lateral line systems," *Bioinspiration Biomimetics*, vol. 8, no. 2, Jun. 2013, Art. no. 026005.
- [20] Y. Yang *et al.*, "Artificial lateral line with biomimetic neuromasts to emulate fish sensing," *Bioinspiration Biomimetics*, vol. 5, no. 1, Mar. 2010, Art. no. 016001.
- [21] X. Zheng *et al.*, "Underwater positioning based on an artificial lateral line and a generalized regression neural network," *J. Bionic Eng.*, vol. 55, no. 5, pp. 883–893, Sep. 2018.
- [22] L. Devries, F. D. Lagor, H. Lei, X. Tan, and D. A. Paley, "Distributed flow estimation and closed-loop control of an underwater vehicle with a multi-modal artificial lateral line," *Bioinspiration Biomimetics*, vol. 10, no. 2, Apr. 2015, Art. no. 025002.
- [23] B. P. Chagnaud and S. Coombs, "Information encoding and processing by the peripheral lateral line system," in *Lateral Line System*. New York, NY, USA: Springer, 2013, vol. 48, pp. 151–194.
- [24] A. T. Abdulsadda and X. Tan, "An artificial lateral line system using IPMC sensor arrays," *Int. J. Smart Nano Mater.*, vol. 3, no. 3, pp. 226–242, Sep. 2012.
- [25] B. J. Wolf and S. M. V. Netten, "Training submerged source detection for a 2D fluid flow sensor array with extreme learning machines," in *Proc. 11th Int. Conf. Mach. Vis.*, 2018, vol. 11041, Art. no. 1104126.
- [26] J. Goulet *et al.*, "Object localization through the lateral line system of fish: Theory and experiment," *J. Comparative Physiol. A*, vol. 194, no. 1, pp. 1–17, Jan. 2008.
- [27] G. Liu, S. Gao, T. Sarkodie-Gyan, and Z. Li, "A novel biomimetic sensor system for vibration source perception of autonomous underwater vehicles based on artificial lateral lines," *Meas. Sci. Technol.*, vol. 29, no. 12, Dec. 2018, Art. no. 125102.
- [28] B. J. Wolf, J. V. D. Wolfshaar, and S. M. V. Netten, "Three-dimensional multi-source localization of underwater objects using convolutional neural networks for artificial lateral lines," *J. Roy. Soc. Interface*, vol. 17, no. 162, Jan. 2020, Art. no. 20190616.

- [29] Y. Jiang, Z. Ma, J. Fu, and D. Zhang, "Development of a flexible artificial lateral line canal system for hydrodynamic pressure detection," *Sensors*, vol. 17, no. 6, Dec. 2017, Art. no. 1220.
- [30] M. Shahinpoor and K. J. Kim, "Ionic polymer-metal composites: I. fundamentals," *Smart Mater. Struct.*, vol. 10, no. 4, pp. 819–833, Aug. 2001.
- [31] H. Lei, C. Lim, and X. Tan, "Modeling and inverse compensation of dynamics of base-excited ionic polymer-metal composite sensors," *J. Intell. Mater. Syst. Struct.*, vol. 24, no. 13, pp. 1557–1571, Sep. 2013.
- [32] Z. Chen, S. Shatara, and X. Tan, "Modeling of biomimetic robotic fish propelled by an ionic polymer-metal composite caudal fin," *IEEE/ASME Trans. Mechatronics*, vol. 15, no. 3, pp. 448–459, Jun. 2010.
- [33] A. T. Abdulsadda and X. Tan, "Underwater source localization using an IPMC-based artificial lateral line," in *Proc. IEEE Int. Conf. Robot. Automat.*, 2011, pp. 2719–2724.
- [34] M. Aureli, C. Prince, M. Porfiri, and S. D. Peterson, "Energy harvesting from base excitation of ionic polymer metal composites in fluid environments," *Smart Mater. Struct.*, vol. 19, no. 1, Jan. 2010, Art. no. 015003.
- [35] J. Wang *et al.*, "The effects of dimensions on the deformation sensing performance of ionic polymer-metal composites," *Sensors*, vol. 19, no. 9, May 2019, Art. no. 2104.
- [36] L. H. Boulogne, B. J. Wolf, M. A. Wiering, and S. M. V. Netten, "Performance of neural networks for localizing moving objects with an artificial lateral line," *Bioinspiration Biomimetics*, vol. 12, no. 5, Oct. 2017, Art. no. 056009.
- [37] S. Samarasinghe, *Neural Networks For Applied Sciences and Engineering: From fundamentals to Complex Pattern Recognition*. Boca Raton, FL, USA: Auerbach, 2007.
- [38] R. A. Fisher, *Statistical Methods for Research Workers*. Edinburgh, U.K.: Oliver and Boyd, 1925.
- [39] V. Bewick, L. Cheek, and J. Ball, "Statistics review 9: One-way analysis of variance," *Crit. Care*, vol. 8, no. 2, pp. 130–136, Apr. 2004.
- [40] S. S. Shapiro and M. B. Wilk, "An analysis of variance test for normality (complete samples)," *Biometrika*, vol. 52, pp. 130–136, 1965.
- [41] H. Levene, "Robust tests for the equality of variance," in *Contributions to Probability and Statistics*, I. Olkin, Ed., Palo Alto, CA, USA: Stanford Univ. Press, 1960, pp. 278–292.
- [42] M. G. Larson, "Analysis of variance," *Circulation*, vol. 117, no. 1, pp. 115–121, 2008.



Yonggang Jiang received the B.S. degree in mechanical engineering from Beihang University, Beijing, China, in 2003, and the M.S. and Ph.D. degrees from the Department of Nanomechanics from Tohoku University, Sendai, Japan, in 2006 and 2009, respectively, both in nanomechanics.

He is currently a Professor with the School of Mechanical Engineering and Automation, Beihang University. His research interests include nano/micro manufacturing, bionic sensing, and

Micro-electromechanical Systems (MEMS).



Zheng Gong received the B.S. degree from the Nanjing University of Aeronautics and Astronautics, Nanjing, China, in 2018, and is currently working toward the Ph.D. degree from the School of Mechanical Engineering and Automation, Beihang University, Beijing, China, both in mechanical engineering.

His research interests include bionic sensing, mechatronics, and sensor fusion.



Zhen Yang received the B.S. degree in automation from China Agricultural University, Beijing, China, in 2020. He is currently working toward the M.S. degree in mechanical engineering from the School of Mechanical Engineering and Automation, Beihang University, Beijing.

His research interests include bionic sensing and sensor fusion.



Zhiqiang Ma received the B.S. degree in engineering from Henan Polytechnic University, Jiaozuo, China, in 2015. He is currently working toward the Ph.D. degree in mechanical engineering from the School of Mechanical Engineering and Automation, Beihang University, Beijing, China.

His research interests include lateral line inspired sensing and biomimetic microsensors.



Chunxuan Wang was born in Shandong, China, in 1974. She received the graduate degree in computer application from Shandong Management University, Jinan, China, in 1998.

She is currently a Chairman with the Shandong Yihang Brake Technology Company, LTD., Shandong, China. Her research interests include vehicle braking system and mechatronics.



Yanjie Wang received the B.S. degree from the China University of Mining and Technology, Xuzhou, China, in 2009, and the Ph.D. degree from Xi'an Jiaotong University, Xi'an, China, in 2015, both in mechanical engineering.

He is currently a Professor with the School of Mechanical and Electrical Engineering, Hohai University, Nanjing, China. His research interests include smart materials and structures, bioinspiration and applied biomimetics, soft robotics, and micro actuating/sensing tech.



Deyuan Zhang (Member, IEEE) received the B.S. and M.S. degrees from the Jilin University of Technology, Changchun, China, in 1984 and 1987, respectively, and the Ph.D. degree from Beihang University, Beijing, China, in 1993, all in mechanical engineering.

He is currently a Professor with the School of Mechanical Engineering and Automation, Beihang University. His research interests include nano/micro/biological manufacturing and ultrasonic vibration cutting.